

Production of dark sector particles via resonant positron annihilation on atomic electrons

Fernando Arias-Aragón,^{1,*} Luc Darmé,^{2,†} Giovanni Grilli di Cortona,^{3,‡} and Enrico Nardi^{1,4,§}

¹*Istituto Nazionale di Fisica Nucleare, Laboratori Nazionali di Frascati, Frascati, 00044, Italy*

²*Institut de Physique des 2 Infinis de Lyon (IP2I),
UMR5822, CNRS/IN2P3, F-69622 Villeurbanne Cedex, France*

³*Istituto Nazionale di Fisica Nucleare, Laboratori Nazionali del Gran Sasso, Assergi, 67100, L'Aquila (AQ), Italy*

⁴*Laboratory of High Energy and Computational Physic,
HEPC-NICPB, Rõvala 10, 10143, Tallin, Estonia*

(Dated: March 25, 2024)

Resonant positron annihilation on atomic electrons provides a powerful method to search for light new particles coupled to e^+e^- . Reliable estimates of production rates require a detailed characterization of electron momentum distributions. We describe a general method that harnesses the target material Compton profile to properly include electron velocity effects in resonant annihilation cross-sections. We additionally find that high Z atoms can efficiently act as particle physics accelerators, providing a density of relativistic electrons that allows to extend by several times the experimental mass reach.

I. INTRODUCTION

Established phenomena like dark matter, the cosmological baryon asymmetry and neutrino masses, which remain unexplained within the Standard Model (SM), provide compelling evidence for the necessity of new physics. Physics beyond the SM may eventually manifest as an entirely novel sector comprising both new particles and interactions. The new states do not need to be particularly heavy to have so far eluded detection; their masses could well be within experimental reach, provided they couple sufficiently feebly to the SM sector.

New light particles with feeble couplings to electron and positrons can be effectively searched for by harnessing intense positron beams impinging on fixed targets. This strategy becomes particularly powerful if the conditions for resonant e^+e^- annihilation into the new states can be engineered, since this would yield a huge enhancement in the production rates. Indeed, the initial proposal for leveraging this strategy [1, 2] has already garnered significant attention within the community [3–9].

Resonant production of new particles requires scanning over suitable center-of-mass energy ranges. This can be achieved in two ways, depending on the characteristics of the target: (i) For thin targets with low nuclear charge, where positron energy losses within the material are negligible, the beam energy must be adjusted incrementally in small steps to continuously span the desired range (see e.g. Ref. [8]); (ii) for thick targets of large nuclear charge, the beam energy can be kept fixed, as the in-matter positron energy losses ensure a continuous energy scan [2]. This applies also to secondary positrons

produced in electromagnetic showers [3, 4, 10, 11] initiated by electron or proton beams. In all cases, a detailed characterization of the momentum distribution of atomic electrons is mandatory to derive reliable estimates of resonant production rates and signal shapes. However, to date, most analyses rely on the simplifying assumption of electrons being at rest. One exception is the original paper [2] where data from the Doppler broadening of the 511 keV photon line from annihilation of stopped positrons [12] were used to account for electron velocity effects in tungsten. While this approach is reasonable, the data considered in [2] describe more properly the annihilation probability distribution of positrons *at rest* as a function of the electron momentum, rather than directly the electrons momentum distribution.¹

In this letter we argue that the Compton profile (CP) (see e.g. [15] for a review) provides an accurate description of the electron momentum distribution for any given material. We describe a prescription for harnessing the CP of a target material to properly incorporate the effects of electron velocities in the cross-section for resonant annihilation. We emphasize that, since the problem at hand involves complicated aspects of solid-state physics, it is crucial to rely on quantities that are experimentally measured. This ensures that theoretical calculations can be directly validated against data. As a concrete example, we consider resonant searches for the elusive X_{17} boson, proposed to explain the anomalies observed in the angular correlation spectra in ^8Be , ^4He and ^{12}C nuclear

* fernando.ariasaragon@lnf.infn.it

† l.darme@ip2i.in2p3.fr

‡ giovanni.grilli@lngs.infn.it

§ enrico.nardi@lnf.infn.it

¹ Recently, modeling that goes beyond the free-electron-at-rest approximation has been incorporated in the computer package DMG4 [13] to simulate new particles production in fixed target experiments. Upon completion of this work, Ref. [14] appeared where atomic binding corrections in lepton-target electron scattering are analyzed. Both these works rely on the virial theorem to estimate electron kinetic energies. However, average electron velocities do not capture the large effects discussed in this paper.

transitions [16–18]. We illustrate the importance of electron velocity effects by estimating the sensitivity of the PADME experiment [19, 20] for X_{17} searches, both in the case of a carbon ($Z = 6$) thin target ($100\mu\text{m}$) (for which data have already been taken and the analysis is ongoing) and for a tungsten ($Z = 74$) thick target (5cm). We then compare our results with previous studies [2, 8]. We anticipate that for the carbon target the effects of electron velocities mainly translate into a certain loss of sensitivity. This is due to the fact that the signal gets spread over a larger range of energies so that the signal-to-noise ratio is decreased.

In the case of the high Z target we observe instead an impressive extension of the reach in mass, by about a factor of four. This is because of head-on collisions with high-momentum electrons in the tail of the momentum distribution allow to reach much higher center-of-mass (CoM) energies than in the case of electrons at rest. This result represents an important finding: it can inspire the conception of suitable experimental setups that, by leveraging this phenomenon, will significantly enhance the mass reach of searches for new particles with positron beams.

II. RESONANT CROSS SECTION

In this work we focus on $2 \rightarrow 1$ processes where a particle X is resonantly produced via positron annihilation on atomic electrons. The differential cross section for positron annihilation off an electron with orbital quantum numbers collectively labeled by q can be written as:

$$d\sigma_q = \frac{d^3p}{(2\pi)^3} \int \frac{d^3k_A}{(2\pi)^3} \int \frac{d^3k_B}{(2\pi)^3} \frac{(2\pi)^4 \delta^{(4)}(k_A + k_B - p)}{2E_X 2E_A 2E_B |v_A - v_B|} \times \frac{|\phi_{A,q}(\mathbf{k}_A)|^2 |\mathcal{M}(k_A, k_B \rightarrow p)|^2 |\phi_B(\mathbf{k}_B)|^2}{(2\pi)^3} \quad (1)$$

where the subscripts A and B label respectively electron and positron quantities, and $\phi(\mathbf{k})$, \mathbf{k} and E denote their wave function, momentum and energy. Note that a subscript q on E_A , v_A and \mathbf{k}_A is left understood. Finally, p and E_X denote the momentum and energy of the final X particle. We take the positrons in the beam as free particles with a well defined momentum \mathbf{p}_B , with a wave function satisfying:

$$\int \frac{d^3k_B}{(2\pi)^3} |\phi_B(\mathbf{k}_B)|^2 = 1, \quad |\phi_B(\mathbf{k}_B)|^2 = (2\pi)^3 \delta^{(3)}(\mathbf{p}_B - \mathbf{k}_B). \quad (2)$$

In contrast, atomic electrons are not free but confined in space, which implies that a certain probability distribution is associated with their momenta. Let us now introduce the electron momentum density function $n(\mathbf{k}_A)$ normalised to the atomic number Z of the target atoms:

$$n(\mathbf{k}_A) = \sum_q |\phi_q(\mathbf{k}_A)|^2, \quad \int \frac{d^3k_A}{(2\pi)^3} n(\mathbf{k}_A) = Z. \quad (3)$$

The electron momentum density distribution $n(\mathbf{k}_A)$ can be directly related to the CP, that is measured from the Doppler shift of scattered photons in the Compton process $e^- + \gamma \rightarrow e^- + \gamma$. This is possible because the time scale for the Compton interaction is much shorter than the time scale needed for the spectator electrons to rearrange in a new configuration, so that the initial and final state electrons feel the same potential. Thus, in this *impulse* approximation, the effect of the binding energies $u_q < 0$ cancels out. However, for the process $e^+e^- \rightarrow X$ the boundary conditions are different, since the X final state does not feel any Coulomb potential and u_q plays a role in energy conservation. Recalling that the positron beam has an intrinsic energy spread $\sigma_B = \delta_B E_B$, it is easy to see that shifts in the CoM become relevant only when $u_q \gtrsim m_e \delta_B \simeq 2.6\text{keV}$, where we have assumed a typical energy spread $\delta_B = 0.5\%$. Thus for low Z materials, and for the outer shell of high Z materials (for tungsten, up to $n \geq 3$), binding energy effects can be neglected. Inner shells of high Z materials can have large binding energies (for tungsten $u_{1s} \sim 70\text{keV}$, $u_{2s,2p} \sim 10 - 12\text{keV}$). However, their contribution to $n(\mathbf{k}_A)$ at low/medium \mathbf{k}_A values is subdominant with respect to the contributions of all other electrons in the outer shells. At large values of \mathbf{k}_A the contribution of the inner shells dominates. However, in this region the momenta of the inner electrons can reach values of order MeV, kinetic energy dominates and the corrections from $u_q \neq 0$ remain small. A prescription to account for binding energies corrections is given in Appendix D. Here, for simplicity, we will neglect u_q in the electron energy-momentum relation. Assuming $E_A \simeq \sqrt{k_A^2 + m_e^2}$ allows to sum Eq. (1) over q to obtain:

$$d\sigma = \frac{d^3p}{(2\pi)^3} \int \frac{d^3k_A}{(2\pi)^3} \frac{(2\pi)^4}{8E_X |E_B k_A^z - E_A p_B^z|} n(\mathbf{k}_A) \times \frac{|\mathcal{M}(k_A, p_B \rightarrow p)|^2 \cdot \delta^{(4)}(k_A + p_B - p)}{(2\pi)^3} \quad (4)$$

where we have used $|v_A - v_B| E_A E_B = |E_B k_A^z - E_A p_B^z|$. We now introduce polar coordinates referred to the beam axis z , with θ_A, ϕ_A denoting the polar and azimuthal angles of \mathbf{k}_A . Integrating over d^3p , we can eliminate three delta functions, after which the conservation conditions read:

$$E_A + E_B = E_X = \sqrt{k_A^2 + p_B^2 + 2k_A p_B x + m_X^2}, \quad (5)$$

with $x = \cos \theta_A$. By leveraging the remaining delta function, we finally obtain:

$$\frac{d^2\sigma}{dk_A d\phi_A} = \frac{|\mathcal{M}|^2}{32\pi^2} \frac{k_A n(k_A, \phi_A, x_0)}{p_B |E_B k_A x_0(k_A) - E_A p_B|}. \quad (6)$$

Energy conservation implies that

$$x_0(k_A) = \frac{2E_A(k_A)E_B + 2m_e^2 - m_X^2}{2k_A p_B}, \quad (7)$$

and the electron momentum k_A lies between:

$$k_A^{\min, \max} = \left| \frac{p_B(2m_e^2 - m_X^2) \pm E_B m_X \sqrt{m_X^2 - 4m_e^2}}{2m_e^2} \right|.$$

Let us now consider a vector particle of mass m_X that couples to electrons through the following interaction:

$$\mathcal{L}_X \subset g_V X_\mu \bar{e} \gamma^\mu e, \quad (8)$$

where g_V is the coupling constant. The spin-averaged matrix element for the resonant process $e^+ e^- \rightarrow X$ is

$$|\mathcal{M}|^2 = g_V^2 (m_X^2 + 2m_e^2). \quad (9)$$

(Eqs. (8) and (9) hold also for dark photon (DP) models with a kinetic mixing parameter $\epsilon = g_V/e$.) Since in this case $|\mathcal{M}|^2$ does not depend on k_A , it can be factored out from the integral in Eq. (4).

III. ELECTRON MOMENTUM DENSITY

The key input for the calculation of the resonant cross-section is the electron momentum distribution $n_A(k_A)$. For most of the elements this quantity has been extracted directly from measurements of the CP [21]. In this Letter, we focus on electron momentum density from spherically averaged Compton profiles, $J(p)$, defined as [22]

$$J(p) = \frac{1}{2} \int_{|p|}^{\infty} \rho(k) k dk, \quad (10)$$

where $\rho(k)$ is the electron momentum distribution normalised as $\int_{-\infty}^{\infty} J(p) dp = Z$ which, in our notation, can be rewritten as $\rho(k) = \frac{n(k)}{2\pi^2}$. The electron momentum density distribution and the CP are then related as:

$$n(k) = -\frac{(2\pi)^2}{k} \frac{dJ(k)}{dk}. \quad (11)$$

The electron momentum distribution of materials can also be obtained from *ab initio* theoretical calculations. Approximate expressions can be derived by using Roothan-Hartree-Fock (RHF) wave functions [23–30], see details in Appendix B.

In the next section we will focus on the PADME experiment [19, 20] that is using a polycrystalline diamond 100 μm target, for which CP data from experiment [31] as well as refined theoretical estimates [22] are available. We extend the k_A range of these CP by using the RHF wave functions method. The electronic structure of carbon is $1s^2 2s^2 2p^2$. However, in the diamond crystal structure one electron is promoted from $2s$ to the $2p$ orbital to increase the covalent bonds. $2s 2p^3$ electrons of one atom then undergo sp^3 hybridization bonding it to four other atoms. RHF wave functions can be used to perform sp^3 hybridization, as detailed in Appendix B.

Besides carbon, we also study the case of a high Z tungsten target, that has the electronic structure $[\text{Xe}] 6s^2 4f^{14} 5d^4$. We use the CP for tungsten from Table I of Ref. [32], and for momenta larger than $p = 7 \text{ a.u.} \simeq 27 \text{ keV}$ up to $p = 100 \text{ a.u.} \simeq 370 \text{ keV}$ we complement those data with the theoretical CP derived in the Dirac Hartree-Fock formalism given in Ref. [33]. For even larger momenta we use the code DBSR-HF [34] to numerically estimate the contribution of the core orbitals up to the $4s$ shell (see Appendix C for more details).

IV. SEARCHES FOR LIGHT NEW BOSONS

Our primary goal is to assess the impact of the motion of atomic electrons on the production of light new bosons via $e^+ e^-$ resonant annihilation. In computing the cross section one must also take into account the energy distribution of positrons in the beam, that can be described by a Gaussian $\mathcal{G}(E, E_B, \sigma_B)$ centered at E_B and with standard deviation σ_B :

$$\sigma_{\text{final}}(E_B, \sigma_B) = \int dE \mathcal{G}(E, E_B, \sigma_B) \sigma(E). \quad (12)$$

In all our computations we have assumed a beam spread $\delta_B \equiv \sigma_B/E_B = 0.5\%$.

We will now focus on the interesting case of the X_{17} boson assuming $m_X = 17 \text{ MeV}$. However, we stress that the effects that we will illustrate do not depend on the nature or mass of the new particle. Figure 1 shows a comparison between cross sections evaluated with different assumptions as a function of the beam energy. Results for a diamond target are given in the left panel, where the blue curve is obtained by assuming electrons at rest, so that the spread is entirely due to σ_B . The orange curve shows the cross section using the RHF approximation, while the green curve is obtained with the CP from [22]. These last two curves are more spread due to the motion of the atomic electrons. The peculiar structure of the green curve is due to the fact that the two core electrons contribute to the broad tails, while the four bond electrons mainly contribute to the central peak. In the right panel we show the same results for tungsten. In this case the cross section exhibits a more significant energy spreading. This is due to the wide range of velocities from high-momentum core electrons. In both cases, the corrected cross-section is starkly different from the electron-at-rest approximation. Clearly, the smearing of the resonance will have an important impact on searches for resonance peaks at fixed target experiments.

In Fig. 2 we show the impact of electron velocities on PADME searches for resonantly produced vector bosons. The PADME sensitivity to X_{17} searches using a thin diamond target is depicted in the left panel, where the reach in the coupling g_V is plotted as a function of m_X . A scan with 12 energy bins covering the range $E_B = [265, 297] \text{ MeV}$ with a total of $6 \cdot 10^{11}$ positrons

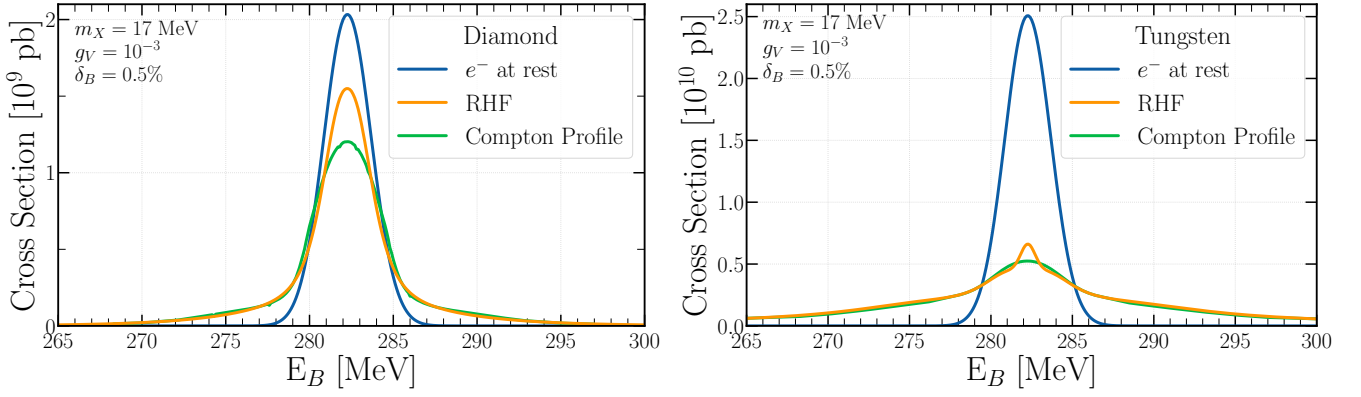


FIG. 1. Cross section for resonant production of a new vector boson with $m_X = 17$ MeV and $g_V = 10^{-3}$, including the effects of positron beam energy spread. The blue curve assumes electrons at rest. The orange curve is obtained with RHF wave functions. The green curve is obtained by using the diamond CP.

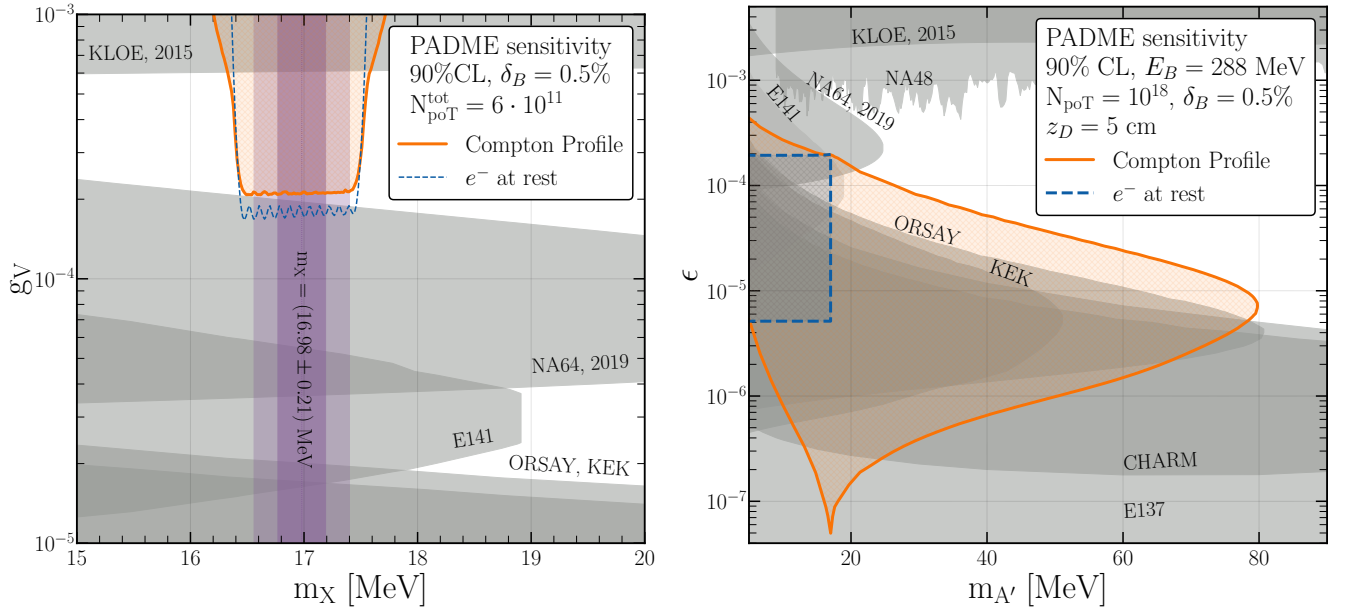


FIG. 2. **Left:** Projected 90% C.L. sensitivity of PADME run-III on g_V as a function of the X_{17} mass assuming atomic electrons at rest (dashed blue) and including electron velocity effects using the diamond CP (solid orange). The dark (light) violet region represents the m_X range from the combined ATOMKI result at 68% (95%) C.L. [16–18]. **Right:** Projected 90% C.L. sensitivity on the DP kinetic mixing parameter ϵ as a function of the DP mass for positrons impinging on a 5 cm thick tungsten target. The dashed blue line assumes electron at rest. The dotted orange line includes electron velocity effects using the tungsten CP. In both plots, the gray shaded regions represent excluded regions (see text).

on target and assuming a 0.5% energy spread, which corresponds to the nominal parameters for the PADME run-III search, has been assumed. The shaded violet regions show the 1σ and 2σ range for $m_X \sim 16.98 \pm 0.21$ MeV from combining the statistical errors from the different ATOMKI measurements [16–18] and adding in quadrature a common systematic error of 0.20 MeV. The gray shaded regions are excluded by KLOE [35], E141 [36], NA64 [37], ORSAY [38] and KEK [39].

The orange line in the left panel shows the projected sensitivity with electron velocity effects included via the CP. The dashed blue line shows, for comparison, the

results previously obtained by assuming electrons at rest [8]. Both these lines have been obtained by assuming a negligible $\gamma\gamma$ background, while 7.5×10^4 background events are expected from s - and t -channel $e^+e^- \rightarrow e^+e^-$. The acceptance was evaluated by requiring that the energy of the final states e^\pm originating from X_{17} decays satisfies $E_\pm > 100$ MeV and the azimuthal angle is in the range $25.5 \lesssim \theta_\pm/\text{mrad} \lesssim 77$, leading to an acceptance of 20% [8]. Systematic uncertainties have been neglected. The plot shows a certain loss in sensitivity once the effect of electron velocities is taken into account. This occurs because the signal becomes distributed over a broader

range of energies, resulting in a reduction of the signal-to-noise ratio.

In the right panel of Fig. 2 the grey regions represent the exclusion limits for DP searches with A' decaying into e^+e^- pairs with unit branching ratio, from the KLOE [35], NA64 [40], ORSAY [38], KEK [39], E137 [3, 41], CHARM [42] and SLAC E141 [36] experiments. The orange region depicts the forecasted 90% C.L. sensitivity (corresponding to ~ 2.7 signal events) achievable with a positron-beam with $E_B = 288$ MeV impinging on a 5 cm-thick tungsten target, assuming a total of 10^{18} poT, in the background-free limit. We see that the contribution of electrons with large momenta allows to probe mass regions that extend to values much larger than one would find assuming electron-at-rest. In fact, practically all of the region from DP masses around 25 MeV up to 80 MeV can be probed thanks to the large tail of the electron momentum distribution. The blue region represents the sensitivity to the X_{17} under the same experimental conditions, but assuming electrons at rest.

V. OUTLOOK AND CONCLUSION

In this work we have discussed a prescription for including the effects of atomic electron momenta in evaluating the cross section for resonant positron annihilation on fixed targets. The electron momentum density can be obtained both from the CP of the target material, or directly from theoretical computation. We have argued that even a relatively simple approach as using RHF wave functions largely improves on the electron-at-rest approximation, as is shown in Fig. 1. We have studied the relevance of these effects in a low Z material (crystalline carbon) as well as in a high Z material, finding in both cases stark differences with the electron-at-rest cross sections. This implies that, in order to obtain reliable quantitative predictions, experiments planning to search for new bosons via their resonant production in fixed targets must necessarily account for atomic electron velocities effects.

This work paves the way for new search strategies where high- Z targets can be leveraged to expand the mass region that can be probed for dark bosons, even when the beam energy is held constant. Indeed, our key finding is that high- Z atoms can behave like particle physics accelerators by providing a non-negligible density of electrons with high momenta that can extend well above the electron mass.

While we have focused on diamond and tungsten targets, for which the electron momentum distribution can be taken as approximately isotropic, our result, Eq. (6), can be applied also to non-isotropic materials. This is important because targets characterised by large anisotropies between different orientations may have a large effect on resonant production rates. Since non-resonant background processes have a much weaker dependence on the electron momentum distribution, it can

be speculated that rotating an anisotropic target into different orientations might help to separate signal from background events. We leave a study of this possibility for future work.

ACKNOWLEDGMENTS

We thank P. Gianotti, M. Raggi, T. Spadaro, P. Valente, and all the members of the PADME collaboration for several useful exchanges regarding the PADME experiment. F.A.A., G.G.d.C. and E.N. were supported by the INFN “Iniziativa Specifica” Theoretical Astroparticle Physics (TAsP), with F.A.A. receiving additional support from an INFN Cabibbo Fellowship, call 2022. L.D. has been supported by the European Union’s Horizon 2020 research and innovation programme under the Marie Skłodowska-Curie grant agreement No 101028626 from 01.09.2021 to 31.08.2023. G.G.d.C. acknowledges LNF and Sapienza University for hospitality at various stages of this work. The work of E.N. was supported by the Estonian Research Council grant PRG1884. We acknowledge support from the CoE grant TK202 “Foundations of the Universe” and from the CERN and ESA Science Consortium of Estonia, grants RVTT3 and RVTT7.

Appendix A: Cross section for resonant production

Without loss of generality, the differential cross section can be written as:

$$d\sigma = \frac{d^3p}{(2\pi)^3} \frac{1}{2E_X} \int d^2b \int \frac{d^3k_A}{(2\pi)^3} \frac{d^3\bar{k}_A}{(2\pi)^3} \int \frac{d^3k_B}{(2\pi)^3} \frac{d^3\bar{k}_B}{(2\pi)^3} \frac{\phi_A(\mathbf{k}_A)\phi_A^*(\bar{\mathbf{k}}_A)}{\sqrt{2E_A 2\bar{E}_A}} \frac{\phi_B(\mathbf{k}_B)\phi_B^*(\bar{\mathbf{k}}_B)}{\sqrt{2E_B 2\bar{E}_B}} e^{-i\mathbf{b}\cdot(\mathbf{k}_B-\bar{\mathbf{k}}_B)} \times_{out} \langle \mathbf{p} | \mathbf{k}_A, \mathbf{k}_B \rangle_{in} \langle \mathbf{p} | \bar{\mathbf{k}}_A, \bar{\mathbf{k}}_B \rangle_{in}^*, \quad (\text{A1})$$

where \mathbf{b} is the impact parameter vector laying in a plane transverse to the beam direction, $\phi(\mathbf{k})$, \mathbf{k} and E represent the wave function, momentum and energy of the electron (positron) when labelled A (B), while p and E_X stand for the final particle momentum and energy; barred variables are used with the exact same meaning as non-barred ones. The integral over the impact factor is straightforward and yields a factor $(2\pi)^2 \delta^{(2)}(\mathbf{k}_B^\perp - \bar{\mathbf{k}}_B^\perp)$, where the superindex is used to indicate the direction of the plane transverse to the beam. The overlap of the initial and final states can be written using the matrix element and energy-momentum conservation (the same applies to the \bar{k}_A and \bar{k}_B momenta), i.e.:

$$_{out} \langle \mathbf{p} | \mathbf{k}_A, \mathbf{k}_B \rangle_{in} = i(2\pi)^4 \delta^{(4)}(k_A + k_B - p) \mathcal{M}, \quad (\text{A2})$$

where \mathcal{M} is the amplitude of the process. Six of the Dirac deltas involving the barred variables can be used to perform the six integrals in the barred momenta. As a result, we have Eq. (1) of the main text:

$$d\sigma = \frac{d^3p}{(2\pi)^3} \int \frac{d^3k_A}{(2\pi)^3} \int \frac{d^3k_B}{(2\pi)^3} \frac{(2\pi)^4 \delta^{(4)}(k_A + k_B - p)}{2E_X 2E_A 2E_B |v_A - v_B|} |\phi_A(\mathbf{k}_A)|^2 |\mathcal{M}(k_A, k_B \rightarrow p)|^2 |\phi_B(\mathbf{k}_B)|^2. \quad (\text{A3})$$

Since the positrons in the beam are free particles with a well defined momentum, their wave function satisfies

$$\int \frac{dk_B^3}{(2\pi)^3} |\phi_B(k_B)|^2 = 1, \quad |\phi_B(k_B)|^2 = (2\pi)^3 \delta^{(3)}(\mathbf{p}_B - \mathbf{k}_B), \quad (\text{A4})$$

which can be used to perform the integral over \mathbf{k}_B . We find

$$d\sigma = \frac{d^3p}{(2\pi)^3} \int \frac{d^3k_A}{(2\pi)^3} \frac{(2\pi)^4}{8E_X |E_B k_A^z - E_A p_B^z|} n(\mathbf{k}_A) |\mathcal{M}(k_A, p_B \rightarrow p)|^2 \cdot \delta^{(4)}(k_A + p_B - p), \quad (\text{A5})$$

where we used $|v_A - v_B| E_A E_B = |E_B k_A^z - E_A p_B^z|$. In Eq. (A5), we have introduced the electron momentum density function $n(\mathbf{k}_A) = \sum_{n,l} |\phi_{n,l}(\mathbf{k}_A)|^2$, normalized to the total number of electrons in the atom $\int \frac{d^3k_A}{(2\pi)^3} n(\mathbf{k}_A) = Z$.

Integrating over d^3p yields

$$\sigma = \frac{1}{32\pi^2} \int d^3k_A \frac{|\mathcal{M}|^2 n(\mathbf{k}_A) \delta(E_A(k_A) + E_B - E_X(\mathbf{k}_A))}{E_X(\mathbf{k}_A) |E_B k_A^z - E_A p_B^z|}, \quad (\text{A6})$$

where $E_A = \sqrt{k_A^2 + m_e^2}$, $E_X = \sqrt{k_A^2 + p_B^2 + 2k_A p_B x + m_X^2}$ and $x = \cos \theta$, with θ the angle formed between \mathbf{p}_B and \mathbf{k}_A .

In the case of an isotropic electron momentum distribution $n(\mathbf{k}_A) = n(k_A)$, after integrating in ϕ and introducing the functions $F(x)$ and $x_0(k_A)$, the solution of the energy conservation,

$$F(k_A, x) = \frac{\partial}{\partial x} (E_A + E_B - E_X) = -\frac{k_A p_B}{E_X(k_A, x)}, \quad x_0(k_A) = \frac{2E_A(k_A)E_B + 2m_e^2 - m_X^2}{2k_A p_B}, \quad (\text{A7})$$

we obtain

$$\sigma = \frac{1}{16\pi} \int_{k_A^{\min}}^{k_A^{\max}} dk_A \frac{|\mathcal{M}|^2 k_A n(k_A)}{p_B |E_B k_A x_0(k_A) - E_A p_B|}. \quad (\text{A8})$$

Energy conservation implies that $-1 \leq x_0 \leq 1$ or equivalently

$$k_A^{\min, \max} = \left| \frac{p_B(2m_e^2 - m_X^2) \pm E_B m_X \sqrt{m_X^2 - 4m_e^2}}{2m_e^2} \right|. \quad (\text{A9})$$

In the typical case where the electron momentum is much smaller than the energy of the positron, we have the approximate relation $k_A^{\min} = m_e \left| 1 - 2m_e \frac{m_e + E_B}{m_X^2} \right|$. This expression vanishes for the resonant condition for a free electron $E_B = E_{res} = \frac{m_X^2}{2m_e} - m_e$. Using this approximation, we have for an isotropic electron momentum distribution:

$$\sigma = \frac{1}{8\pi} \frac{1}{E_B(m_X^2 - 2m_e^2)} \int_{k_A^{\min}}^{\infty} dk_A |\mathcal{M}|^2 k_A n(k_A). \quad (\text{A10})$$

When $|\mathcal{M}|^2$ does not depend on k_A , the cross-section can be factorised into a term computed from Feynman diagrams and a form factor which depends on the electron momentum density distribution.²

Appendix B: Electron momentum density distribution in diamond

The main variable in the result in (A8) is the electron momentum density function $n_A(k_A)$.

a. Roothan-Hartree-Fock wave functions The RHF equations describe the atomic wave functions, characterized by the principal, azimuthal and magnetic quantum numbers n , ℓ and m , by separating the radial and angular part. The angular part is described by the spherical harmonics (in the Condon-Shortley phase convention [43]) $Y_\ell^m(\hat{x})$, while the radial one is described in terms of Slater-type orbitals (STO) [44]:

$$R(r, Z, n) = a_0^{-3/2} \frac{(2Z)^{n+1/2}}{\sqrt{(2n)!}} \left(\frac{r}{a_0} \right)^{n-1} e^{-\frac{Zr}{a_0}}, \quad (\text{B1})$$

with a_0 the Bohr radius and Z the effective nuclear charge. The atomic wave function can then be written as:

$$\psi_{n\ell m}^{\text{atom}}(\vec{x}) = \sum_j C_{j\ell n} R(r, Z_{j\ell}, n_{j\ell}) Y_\ell^m(\hat{x}), \quad (\text{B2})$$

where $C_{j\ell n}$, $Z_{j\ell}$ and $n_{j\ell}$ are tabulated e.g. in Refs. [45, 46]. The Fourier transform of this wave function can be computed analytically [47].

b. Fourier transform of the wave function The Fourier transform of the Roothan-Hartree-Fock Slater Type Orbital wave function in equation (B2) can be written analytically [47]:

$$\begin{aligned} \tilde{\psi}_{n\ell m}^{\text{atom}}(\vec{q}) &= \sum_j C_{j\ell n} \int \frac{d^3x}{(2\pi)^3} e^{i\vec{q}\cdot\vec{x}} R(x, Z_{j\ell}, n_{j\ell}) Y_\ell^m(\hat{x}) = \sum_j C_{j\ell n} \tilde{\chi}(q, Z_{j\ell}, n_{j\ell}, \ell) Y_\ell^m(\hat{q}) \\ \tilde{\chi}(q, Z_{j\ell}, n_{j\ell}, \ell) &= a_0^{3/2} \frac{2^{n_{j\ell}-1} (n_{j\ell} - \ell)!}{\pi^2} (ia_0 q)^\ell Z_{j\ell}^{n_{j\ell}-\ell} \frac{(2Z_{j\ell})^{n_{j\ell}+1/2}}{\sqrt{(2n_{j\ell})!}} \sum_{s=0}^{\lfloor (n_{j\ell}-\ell)/2 \rfloor} \frac{\omega_s^{n_{j\ell}\ell}}{((a_0 q)^2 + Z_{j\ell}^2)^{n_{j\ell}-s+1}}, \\ \omega_s^{n_{j\ell}\ell} &= (-4Z_{j\ell}^2)^{-s} \frac{(n_{j\ell} - s)!}{s!(n_{j\ell} - \ell - 2s)!}, \end{aligned} \quad (\text{B3})$$

where the upper limit $\lfloor (n_{j\ell} - \ell)/2 \rfloor$ in the summation denotes the floor of $(n_{j\ell} - \ell)/2$, i.e., the largest integer less or equal to the argument, where the coefficients $C_{j\ell n}$, $n_{j\ell}$ and $Z_{j\ell}$ can be found in Ref. [45, 46], while Y_ℓ^m are the spherical harmonics with the Condon-Shortley phase convention and a_0 is the Bohr radius.

c. Hybridization for diamond The electronic structure of carbon in diamond is $1s^2 2s^1 2p^3$, with the valence electrons exhibiting sp^3 hybridization. We can then construct the electron wave functions for the $n = 2$ electrons:

$$\begin{aligned} \psi_{sp3a}^{\text{atom}} &= \tilde{\psi}_{20(0)}^{\text{atom}} + \tilde{\psi}_{21(+1)}^{\text{atom}} + \tilde{\psi}_{21(0)}^{\text{atom}} + \tilde{\psi}_{21(-1)}^{\text{atom}}, \\ \psi_{sp3b}^{\text{atom}} &= \tilde{\psi}_{20(0)}^{\text{atom}} + \tilde{\psi}_{21(+1)}^{\text{atom}} - \tilde{\psi}_{21(0)}^{\text{atom}} - \tilde{\psi}_{21(-1)}^{\text{atom}}, \\ \psi_{sp3c}^{\text{atom}} &= \tilde{\psi}_{20(0)}^{\text{atom}} - \tilde{\psi}_{21(+1)}^{\text{atom}} - \tilde{\psi}_{21(0)}^{\text{atom}} + \tilde{\psi}_{21(-1)}^{\text{atom}}, \\ \psi_{sp3d}^{\text{atom}} &= \tilde{\psi}_{20(0)}^{\text{atom}} - \tilde{\psi}_{21(+1)}^{\text{atom}} + \tilde{\psi}_{21(0)}^{\text{atom}} - \tilde{\psi}_{21(-1)}^{\text{atom}}. \end{aligned}$$

On the other hand, the $1s$ electrons remain in their RHF STO form defined in equation (B3).

² The limit of free electrons at rest can be recovered from Eq. (A10) by replacing n_A with a delta-function (similar to Eq. (2)) multi-

plied by Z , and by sending $k_A \rightarrow 0$.

Appendix C: Electron momentum density distribution in large-Z materials

For large-Z material, the core electrons are typically relativistic and the study of the large momentum limit should thus rely on relativistic quantum mechanical methods. Fortunately, several state-of-the art numerical codes are available. We used in particular codes based on the Dirac-Hartree-Fock (DHF) method. In the case of a Coulomb-like potential (and thus a point-like nuclei), the results for the Dirac wave function are well-known and can be found in various textbooks (see e.g. [48] chap. 14).

Various improvements have been made throughout the years, in particular with a better description of the charge density inside the nucleus, various interaction terms between electrons and a modelisation of QED corrections (for a recent review, see for instance [49]). We rely on the implementation of these effects in the codes GRASP18 [50, 51] and DBSR-HF [34]. More precisely, these codes are used to find the “large” and “little” radial wave functions components (resp. $P(r)$ and $Q(r)$) for each orbital. The momentum density distribution is then obtained as:

$$\rho_q(k) = N_q(|\gamma_{q,P}|^2 + |\gamma_{q,Q}|^2) \quad (\text{C1})$$

where N_q is the number of electrons in each orbital and q refers to the DHF orbitals. Note that the latter are which split with respect to the non-relativistic case due to the spin-orbit contributions linking the orbital moment ℓ and electron spin³. We also introduced $\gamma_{q,P}$ and $\gamma_{q,Q}$ which are integrals over the radius r . For the orbitals s and p we have:

$$\gamma_P(k) = \sqrt{\frac{2}{\pi}} \int_0^\infty P(r) j_\ell(kr) dr \quad (\text{C2})$$

where $\ell = 0, 1$ for s, p shells and j_ℓ is a spherical Bessel function of the first kind. For γ_Q , we have:

$$\gamma_Q(k) = \sqrt{\frac{2}{\pi}} \int_0^\infty Q(r) j_{\ell_i}(kr) dr \quad \text{with } \ell_i = \begin{cases} 1 & \text{for s shells} \\ 0 & \text{for p- shells} \\ 2 & \text{for p shells} \end{cases} \quad (\text{C3})$$

The d and higher shells behave as the p shell, with e.g. $\ell_i = \ell - 1 = 1$ for the $d-$ and $\ell_i = \ell + 1 = 3$ for the d . We have cross-checked that the output of both GRASP18 and DBSR-HF agreed to an excellent level (being based on the same theoretical foundations) in the relevant large momentum regime. We further illustrate the matching between the different approaches in Fig. 3, where we have represented the Compton profiles as found both from [33] and DBSR-HF [34]. We find a percent level agreement at momenta around 0.25 MeV where we switch from one to the other.

³ We use the same notation as in the outputs of the above atomic physics codes. For instance, there are 2 states in the s -shells, 2

in $p-$ shells, 4 in p shells, 4 in $d-$ shells and 6 in d shells.

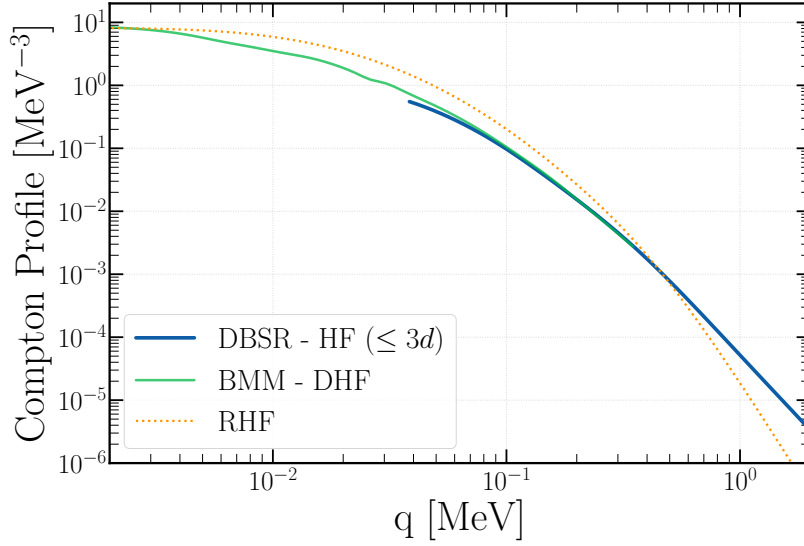


FIG. 3. Matching between the different approaches to the electron density distribution at large momentum, represented in term of the isotropic Compton profile $J(q)$. The green line is the DHF as extracted from [33], the blue line the result from DBSR-HF [34]. We show for comparison the non-relativistic HF from [46] in dotted orange.

Appendix D: Effects of electron binding energies

The result from App. B can be easily adapted to account for the binding energy of the electrons. For each shell with binding energy $u_q < 0$, the energy E_A of the electron is now linked to its momentum via:

$$E_A = \sqrt{k_A^2 + m_e^2} + u_q, \quad (\text{D1})$$

For the hydrogen-like atoms, exact expressions for the negative binding energies exist [48]. For more general cases, they can be evaluated via numerical codes like GRASP [33] or DBSR-HF [34] or simply from tabulated data (e.g. Ref. [52]).

The procedure described in App. A does not rely on Eq. (D1), up to the expression for $x_0(k_A)$, which becomes

$$x_{0,u_q}(k_A) = \frac{2E_A(k_A)E_B + 2m_e^2 - m_X^2 + (u_q(2E_A - u_q))}{2k_A p_B} \simeq \frac{2E_A(k_A)E_B + 2m_e^2 - m_X^2}{2k_A p_B}, \quad (\text{D2})$$

where in the last line, we have used the hierarchy $u_q \ll E_A \ll E_B$, which is always satisfied in the setups relevant to this work. Thus we recover precisely the expression from the main text, up to fact that the energy is now defined as Eq. (D1). The kinematic boundaries can be similarly easily found. In the above limit, we have the simple expressions

$$k_{A,u_q}^{\min,\max} = \left| \frac{p_B(2m_e^2 - \tilde{m}_X^2) \pm E_B \tilde{m}_X \sqrt{\tilde{m}_X^2 - 4m_e^2}}{2m_e^2} \right|, \quad \text{with } \tilde{m}_X^2 = m_X^2 - 2E_B u_q, \quad (\text{D3})$$

where we have only kept $E_B u_q$ correction terms. Thus the main effect of the binding energies is to shift the resonant mass condition, which becomes at first order

$$E_{res,b} = \frac{m_X^2}{2m_e} \left(1 - \frac{u_q}{m_e} \right) - m_e. \quad (\text{D4})$$

This amounts to a 0.06% shift for the 1s shell of Carbon (with $u_{A1s} = -300$ eV) and a 13% shift for the 1s of Tungsten (with $u_{1s} = -69$ keV).

Our final result for the integrated cross-section thus requires to sum over all the shells with different energy levels

$$\sigma = \sum_q \frac{|\mathcal{M}|^2}{16\pi} \int_{k_{A,u_q}^{\min}}^{k_{A,u_q}^{\max}} dk_A \frac{k_A n_q(k_A)}{p_B |E_B k_A x_{0,u_q}(k_A) - E_A p_B|}, \quad (\text{D5})$$

where $q = 1s, 2s, 2p-, 2p \dots$ represents the DHF shells as described in App. (C) and $n_q(k) = (2\pi^2)\rho_q(k)$.

In practice however, significant effects occur only in large- Z material for the inner-most shells around the resonance (for which k^{\min} tends to zero). While we included this effect for the $1s$ shell for Tungsten, we found the corresponding modification of the projected limits almost unchanged in the not-yet excluded part of the parameter space. As discussed in the main text this is simply the consequence of the fact that for masses around the resonance (thus with $k^{\min} \rightarrow 0$), the signal mostly arise from weakly bound – valence electrons – orbitals, while for larger masses the correction terms in Eq. (D3) become again negligible due to their suppression by m_X^2 .

Appendix E: Signal events in a thick target

The number of DP events in a thick target with atomic number Z and mass number A is given by [2]:

$$N_{A'} = \frac{N_{\text{poT}} N_{\text{Av}} X_0 \rho}{A} \int_0^T dt \mathcal{P}(t, z_D, z_{\text{det}}, \ell_\epsilon) \int dE_e \int dE \mathcal{G}(E, E_e, \sigma_{E_e}) I(E, E_e, t) \sigma(E_e), \quad (\text{E1})$$

with N_{poT} the number of positron on target, N_{Av} the Avogadro number, X_0 the radiation length ($X_0 = 3.5$ mm for tungsten), T the target length in unit of radiation length and ρ the density ($\rho = 19.3$ g/cm³ for tungsten). The probability that the DP decays between the production point and the detector is

$$\mathcal{P}(t, z_D, z_{\text{det}}, \ell_\epsilon) = e^{\frac{X_0 t - z_D}{\ell_\epsilon}} \left(1 - e^{\frac{X_0 t - z_{\text{det}}}{\ell_\epsilon}} \right), \quad (\text{E2})$$

where z_D is the target length, z_{det} is the distance between the origin and the detector, and $\ell_\epsilon = \gamma c \tau_{A'}$ is the DP decay length. In this case, the decay length depends explicitly on the atomic electron momentum via $\gamma = E_X(k)/m_X$ with E_X given by Eq. (5), and $\tau_{A'} = 1/\Gamma_{A'}$ is the DP lifetime with

$$\Gamma_{A'} = \frac{\epsilon^2 \alpha}{3} m_{A'} \left(1 + 2 \frac{m_e^2}{m_{A'}^2} \right) \sqrt{1 - 4 \frac{m_e^2}{m_{A'}^2}}.$$

The Gaussian $\mathcal{G}(E, E_B, \sigma_B)$ describes the energy distribution of positron inside the beam. Finally, the probability of finding a positron with energy E_e after passing through $t = z/X_0$ radiation lengths is [53, 54]

$$I(E, E_e, t) = \frac{\theta(E - E_e)}{E\Gamma(bt)} \left(\log \frac{E}{E_e} \right)^{bt-1}, \quad (\text{E3})$$

where $b = 4/3$, E is the initial energy before the target and Γ is the Gamma function.

-
- [1] E. Nardi, in *New directions in Dark Matter and Neutrino Physics*, Perimeter Institute, July 20-22, 2017, (PI Video Library: <http://pirsa.org/17070015>).
 - [2] E. Nardi, C. D. R. Carvajal, A. Ghoshal, D. Meloni, and M. Raggi, *Phys. Rev. D* **97**, 095004 (2018), [arXiv:1802.04756 \[hep-ph\]](#).
 - [3] L. Marsicano, M. Battaglieri, M. Bondi', C. D. R. Carvajal, A. Celentano, M. De Napoli, R. De Vita, E. Nardi, M. Raggi, and P. Valente, *Phys. Rev. D* **98**, 015031 (2018), [arXiv:1802.03794 \[hep-ex\]](#).
 - [4] A. Celentano, L. Darmé, L. Marsicano, and E. Nardi, *Phys. Rev. D* **102**, 075026 (2020), [arXiv:2006.09419 \[hep-ph\]](#).
 - [5] M. Battaglieri *et al.*, *Eur. Phys. J. A* **57**, 253 (2021), [arXiv:2105.04540 \[hep-ex\]](#).
 - [6] Y. M. Andreev *et al.*, *Phys. Rev. D* **104**, L091701 (2021), [arXiv:2108.04195 \[hep-ex\]](#).
 - [7] M. Battaglieri *et al.*, *Phys. Rev. D* **106**, 072011 (2022), [arXiv:2208.01387 \[hep-ex\]](#).
 - [8] L. Darmé, M. Mancini, E. Nardi, and M. Raggi, *Phys. Rev. D* **106**, 115036 (2022), [arXiv:2209.09261 \[hep-ph\]](#).
 - [9] D. S. M. Alves *et al.*, *Eur. Phys. J. C* **83**, 230 (2023).
 - [10] L. Marsicano, M. Battaglieri, M. Bondi', C. D. R. Carvajal, A. Celentano, M. De Napoli, R. De Vita, E. Nardi, M. Raggi, and P. Valente, *Phys. Rev. Lett.* **121**, 041802 (2018), [arXiv:1807.05884 \[hep-ex\]](#).
 - [11] L. Darmé, *Phys. Rev. D* **106**, 055015 (2022), [arXiv:2205.09773 \[hep-ph\]](#).
 - [12] V. J. Ghosh, M. Alatalo, P. Asoka-Kumar, B. Nielsen, K. G. Lynn, A. C. Kruseman, and P. E. Mijnders, *Phys. Rev. B* **61**, 10092 (2000).
 - [13] B. B. Oberhauser *et al.*, (2024), [arXiv:2401.12573 \[hep-ph\]](#).
 - [14] R. Plestid and M. B. Wise, (2024), [arXiv:2403.12184 \[hep-ph\]](#).

- [15] B. G. Williams and J. M. Thomas, *International Reviews in Physical Chemistry* **3**, 39 (1983), <https://doi.org/10.1080/01442358309353339>.
- [16] A. J. Krasznahorkay *et al.*, *Phys. Rev. Lett.* **116**, 042501 (2016), arXiv:1504.01527 [nucl-ex].
- [17] A. J. Krasznahorkay *et al.*, *J. Phys. Conf. Ser.* **1056**, 012028 (2018).
- [18] A. J. Krasznahorkay, M. Csatlós, L. Csige, J. Gulyás, A. Krasznahorkay, B. M. Nyakó, I. Rajta, J. Timár, I. Vajda, and N. J. Sas, *Phys. Rev. C* **104**, 044003 (2021), arXiv:2104.10075 [nucl-ex].
- [19] M. Raggi and V. Kozhuharov, *Adv. High Energy Phys.* **2014**, 959802 (2014), arXiv:1403.3041 [physics.ins-det].
- [20] M. Raggi, V. Kozhuharov, and P. Valente, *EPJ Web Conf.* **96**, 01025 (2015), arXiv:1501.01867 [hep-ex].
- [21] M. J. Cooper, *Reports on Progress in Physics* **48**, 415 (1985).
- [22] J. C. Aguiar, C. R. Quevedo, J. M. Gomez, and H. O. Di Rocco, *Physica B Condensed Matter* **521**, 361 (2017).
- [23] S. Huzinaga, *The Journal of chemical physics* **42**, 1293 (1965).
- [24] E. Steinborn and K. Ruedenberg, in *Advances in quantum chemistry*, Vol. 7 (Elsevier, 1973) pp. 1–81.
- [25] E. Clementi and C. Roetti, *Atomic data and nuclear data tables* **14**, 177 (1974).
- [26] P. Kaijser and V. H. Smith Jr, in *Advances in quantum chemistry*, Vol. 10 (Elsevier, 1977) pp. 37–76.
- [27] E. Filter and E. O. Steinborn, *Physical Review A* **18**, 1 (1978).
- [28] D. K. Maretis, *The Journal of Chemical Physics* **71**, 917 (1979).
- [29] E. J. Weniger and E. O. Steinborn, *The Journal of Chemical Physics* **78**, 6121 (1983).
- [30] E. J. Weniger, *Journal of mathematical physics* **26**, 276 (1985).
- [31] R. J. Weiss and W. C. Phillips, *Phys. Rev.* **176**, 900 (1968).
- [32] U. Mittal, B. K. Sharma, F. M. Mohammad, and B. L. Ahuja, *Phys. Rev. B* **38**, 12208 (1988).
- [33] F. Biggs, L. Mendelsohn, and J. Mann, *Atomic Data and Nuclear Data Tables* **16**, 201 (1975).
- [34] O. Zatsarinny and C. Froese Fischer, *Computer Physics Communications* **202**, 287 (2016).
- [35] A. Anastasi *et al.*, *Phys. Lett. B* **750**, 633 (2015), arXiv:1509.00740 [hep-ex].
- [36] E. M. Riordan *et al.*, *Phys. Rev. Lett.* **59**, 755 (1987).
- [37] Y. M. Andreiev *et al.* (NA64), *Phys. Rev. D* **104**, L111102 (2021), arXiv:2104.13342 [hep-ex].
- [38] M. Davier and H. Nguyen Ngoc, *Phys. Lett. B* **229**, 150 (1989).
- [39] A. Konaka *et al.*, *Phys. Rev. Lett.* **57**, 659 (1986).
- [40] E. Depero *et al.* (NA64), *Eur. Phys. J. C* **80**, 1159 (2020), arXiv:2009.02756 [hep-ex].
- [41] S. Andreas, C. Niebuhr, and A. Ringwald, *Phys. Rev. D* **86**, 095019 (2012), arXiv:1209.6083 [hep-ph].
- [42] Y.-D. Tsai, P. deNiverville, and M. X. Liu, *Phys. Rev. Lett.* **126**, 181801 (2021), arXiv:1908.07525 [hep-ph].
- [43] E. Condon and G. Shortley, *The Theory of Atomic Spectra*, Cambridge Univ.Pr.209 (Cambridge University Press, 1935).
- [44] J. C. Slater, *Phys. Rev.* **36**, 57 (1930).
- [45] C. F. Bunge, J. A. Barrientos, and A. V. Bunge, *Atom. Data Nucl. Data Tabl.* **53**, 113 (1993).
- [46] A. D. McLean and R. S. McLean, *Atom. Data Nucl. Data Tabl.* **26**, 197 (1981).
- [47] D. Belkić and H. S. Taylor, *Physica Scripta* **39**, 226 (1989).
- [48] H. A. Bethe and E. E. Salpeter, *Quantum Mechanics of One- and Two-Electron Atoms* (1957).
- [49] O. R. Smits, P. Indelicato, W. Nazarewicz, M. Piibeleht, and P. Schwerdtfeger, *Physics Reports* **1035**, 1 (2023).
- [50] P. Jönsson, G. Gaigalas, J. Bieroń, C. F. Fischer, and I. Grant, *Computer Physics Communications* **184**, 2197 (2013).
- [51] C. Froese Fischer, G. Gaigalas, P. Jönsson, and J. Bieroń, *Computer Physics Communications* **237**, 184 (2019).
- [52] J. A. BEARDEN and A. F. BURR, *Rev. Mod. Phys.* **39**, 125 (1967).
- [53] H. Bethe and W. Heitler, *Proc. Roy. Soc. Lond. A* **146**, 83 (1934).
- [54] Y.-S. Tsai and V. Whitis, *Phys. Rev.* **149**, 1248 (1966).